NANO LETTERS

Letter

pubs.acs.org/NanoLett

Heterogeneity in the Small-Scale Deformation Behavior of Disordered Nanoparticle Packings

Joel A. Lefever,[†] Tevis D. B. Jacobs,[†] Qizhan Tam,[‡] Jyo Lyn Hor,[§] Yun-Ru Huang,[§] Daeyeon Lee,[§] and Robert W. Carpick*[,‡]

[†]Department of Materials Science & Engineering, University of Pennsylvania, Philadelphia, Pennsylvania 19104, United States

[‡]Department of Mechanical Engineering & Applied Mechanics, University of Pennsylvania, Philadelphia, Pennsylvania 19104, United States

[§]Department of Chemical & Biomolecular Engineering, University of Pennsylvania, Philadelphia, Pennsylvania 19104, United States

Supporting Information

ABSTRACT: Atomic force microscopy-based nanoindentation is used to image and probe the local mechanical properties of thin disordered nanoparticle packings. The probed region is limited to the size of a few particles, and an individual particle can be loaded and displaced to a fraction of a single particle radius. The results demonstrate heterogeneous mechanical response that is location-dependent. The weak locations may be analogous to the "soft spots" previously predicted in glasses and other disordered packings.

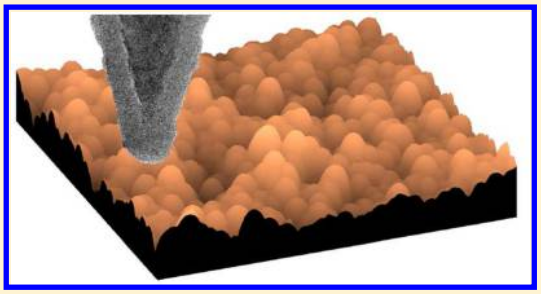

KEYWORDS: *Disordered nanoparticle packing, amorphous material, atomic force microscopy, nanoindentation, soft spot, shear transformation zone*

Amorphous materials are becoming increasingly common in a number of applications, including microelectromechanical systems,[1,2] optical and protective coatings,[3,4] solar cells,[5] electronics,[6] and proposed for biomedical applications.[6,7] In these applications, the lack of grain structure enables small or thin structures to be fabricated with extremely smooth and conformal surfaces and can also result in excellent tribological properties.[8,9] Amorphous systems can range from atomic glasses to colloidal and granular systems. This includes nanoparticle packings, which have significant practical relevance. For example, certain types of nanoparticle packings have been demonstrated to have useful optical antireflection properties, as well as superhydrophilicity which can prevent fogging.[4] In addition, as porous materials, they have high surface area, making them useful functional materials, such as for electrochemistry.[10] Although interest in these materials has grown significantly, approaches for characterizing their mechanical behavior are lacking, and their mechanical failure mechanisms are not well-understood. Disordered nanoparticle packings are a convenient system for analysis of deformation modes in amorphous materials because the length scale is small enough that interparticle forces remain relevant, while, unlike in atomic glasses, the particles themselves can be resolved. In this study, we investigate the mechanical properties and deformation mechanisms of nanoparticle packings using atomic force microscopy both to image and also to elastically and plastically deform the system.

The physics of amorphous materials over a wide range of length scales have been shown to share certain similarities, especially in their mechanical deformation and failure mechanisms.[11−13] Such a system is said to be "jammed" if the material is compressed tightly enough that it remains rigid.[12] In this condition, the atoms in the interior of the system are held in place by their neighbors, providing a restoring force in all directions. An externally applied stress can modify the shape of the potential energy landscape until the energy barrier for some particular atomic-level rearrangement is sufficiently reduced that the rearrangement occurs.

Computational simulations of disordered packings have revealed that the frequencies and density of vibrational states may correlate with their local structure and mechanical properties.[11,14] The lowest-frequency vibrational modes in the system tend to be quasi-localized, exciting atoms in particular regions more than elsewhere. These regions represent sites where the restoring forces are weak, and have been labeled as soft spots;[14] typically, they are approximately 10 particles in size. Under an applied strain, some of these vibrational modes reduce to zero, indicating a complete disappearance of one of the restorative forces in the system.

In the simulations, the reduction of a vibrational frequency to zero leads to a structural instability that results in a rearrangement of a few atoms. These rearrangements are consistent with the hypothesized shear transformation zones or STZs. These rearrangements of a few atoms are believed to be

Received: December 31, 2015
Revised: March 5, 2016
Published: March 15, 2016

DOI: 10.1021/acs.nanolett.5b05319
Nano Lett. 2016, 16, 2455−2462

the fundamental units of plastic deformation in metallic glasses and other disordered materials,[15] akin to the way that dislocations are the units of plastic deformation in crystalline metals. Unlike dislocations, however, an STZ rearrangement is an event which leaves behind no observable evidence of its occurrence. Whereas a dislocation can be imaged using transmission electron microscopy or inferred at the surface by the existence of discrete atomic steps, an STZ rearrangement must be witnessed in action or imaged before and after its occurrence. This is extremely challenging in experimental work because it is not generally possible to predict where an STZ will occur. STZs have been witnessed in simulations[16] and in large-scale experimental systems such as bubble rafts[17] and disordered colloids.[18] While they are hypothesized to occur at soft spots, to date only limited work has attempted to identify soft spots spatially in real atomic-scale systems.[19,20] Moreover, once an STZ has actuated, it often causes an avalanche of events propagating at close to the speed of sound, leading to the formation of a shear band.[21,22] Therefore, observing a single STZ in an experiment is difficult not only due to the challenge of predicting where it will occur, but also because it is difficult to isolate a single STZ temporally.

Disordered nanoparticle packings are sufficiently small that van der Waals and other physicochemical interactions can still be significant. This property makes them an appealing analogue for atomic glasses, with the advantage that individual constituents, i.e., the nanoparticles, act like "artificial atoms" which are readily imageable. Nanoparticle packings are also beneficial in this context because, in principle, it is feasible to perturb a nanoparticle packing by a deflection that is small compared to the particle radius and measure the ensuing deformation with subparticle size resolution. This reduces the likelihood of unintentionally instigating a cascade effect; by contrast, it is exceptionally difficult to apply a load to a single atom in a metallic glass. Although nanoparticle packings at this length scale have never been used to gain particle-level resolution of STZs, conventional nanoindentation has shown that they develop shear bands at the mesoscale,[23] thus demonstrating a similarity in deformation modes between nanoparticle packings and metallic glasses. In addition, conventional nanoindentation is capable of estimating the density of defects in a metallic glass;[24,25] however, this technique cannot pinpoint the location of soft spots or STZs because of its limited lateral spatial resolution as compared with scanning probe techniques.

Recently the mechanical properties of disordered nanoparticle films have been characterized using conventional indentation techniques, demonstrating that they exhibit properties of both granular and viscoplastic materials.[26] For example, nanoindentation revealed that atomic layer deposition may be used to strengthen nanoparticle packings.[27,28] Nanoindentation experiments also showed that particle shape anisotropy causes an increase in toughness and a reduction in the stiffness of nanoparticle packings.[23] However, the fundamental deformation and failure mechanisms of nanoparticle packings due to external stress, such as resulting from nanoindentation, have not yet been determined.

In the present study, nanoindentation was performed on nanoparticle packings using atomic force microscopy (AFM). With its nanometer-scale spatial resolution, AFM is able to probe the mechanical heterogeneities hypothesized to occur in amorphous materials. Since soft spots are favorable at free surfaces,[29] there is an increased likelihood of finding them with AFM-based mechanical measurements that probe the surface of the nanoparticle packing. We find that those nanoparticles with a strong mechanical connection to the substrate[30] can be identified with AFM nanoindentation.

Thin films were prepared by spin-coating from a 5% by weight aqueous colloidal solution of 20.0 ± 4.8 nm diameter SiO_2 nanoparticles with thin alumina coatings (LUDOX CL, Sigma-Aldrich, St. Louis, MO) onto a silicon wafer. The particle size was confirmed by both transmission and scanning electron microscopy as well as dynamic light scattering. The alumina coating produces a smoother, rounder particle than found for pure SiO_2, which produces a better analogue to atomic glasses. The films were deposited onto a silicon wafer by spin-coating at 1500 rpm, which produces an approximately 100 nm thick film as determined by ellipsometry. Thicker films were prepared by repeating this process multiple times, which was necessary to suppress cracking.[31]

Films were imaged using an AFM (Icon, Bruker, Boston, MA) with a silicon tapping-mode probe coated with a diamond-like carbon film (Tap300DLC, BudgetSensors, Sofia, Bulgaria). The spring constant of the probe was calibrated by performing multiple indents along the length of a reference cantilever with a known spring constant (CLFC, Veeco, Inc.). AFM nanoindentation was performed to maximum forces in a range from 100 to 800 nN, yielding data about the deflection of the cantilever as a function of the position of its base. A typical force curve is shown in Figure 2a, with the deflection of the probing cantilever subtracted from the position of the cantilever base, so the deflection axis represents the deflection of the sample only. From this force−displacement curve, mechanical properties were determined using the methods outlined in ref 32.

Amplitude modulation AFM (AM-AFM; also known as tapping mode) topographic imaging was used to characterize the surface of the film, to ensure that the region of interest is flat at the particle level and free of contamination. In addition, this technique was used to determine the exact positions of nanoparticles in the film with subnanometer resolution. Drive amplitudes, set point, scan size and resolution, and feedback gains were all tuned to yield high-quality scans with minimal noise or damage to the sample and tip; typical values are given in Table S1 in the Supporting Information. A typical topography scan is shown in Figure 1a, where the entire 500 nm × 500 nm scan has a root-mean-square (RMS) roughness of 2.23 nm, or 2.11 nm after line-by-line flattening has been applied. Over a collection of ten 500 nm scans, the RMS roughness was 2.97 ± 0.30 nm, or 2.41 ± 0.21 nm with line-by-

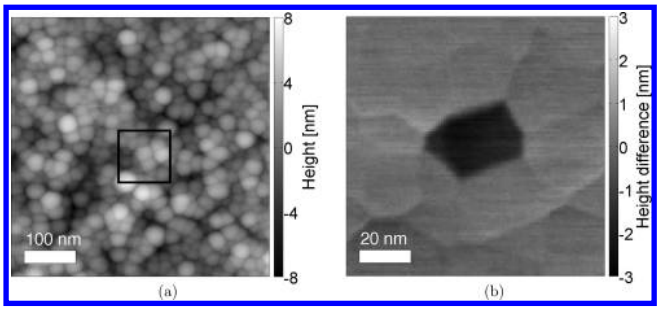

Figure 1. (a) Topography of a film of silica nanoparticles taken using tapping-mode AFM before performing indentations. (b) A subset of the difference image between the before and after scans (black square in a), showing the disturbed region limited to a single particle size.

DOI: 10.1021/acs.nanolett.5b05319
Nano Lett. 2016, 16, 2455−2462

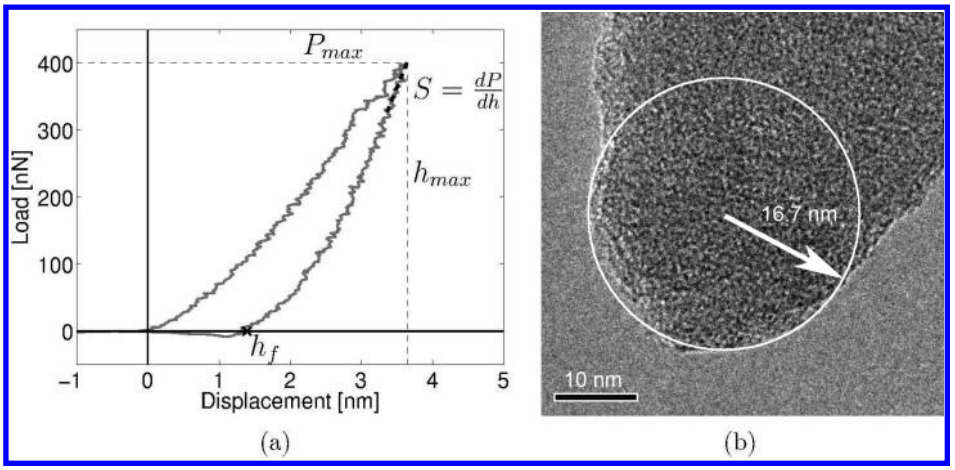

Figure 2. (a) An example force curve, showing an indentation on a 105 nm thick SiO_2 nanoparticle film. (b) Transmission electron micrograph of one of the AFM probe tips used in this study. The best-fit circle to the tip geometry is indicated in white and has a radius of 16.7 nm.

line flattening. This is well below the particle diameter of 21 nm, indicating an extremely smooth film. The RMS roughness is affected by imaging artifacts resulting from tip convolution, which tend to reduce the measured roughness below that of a particle radius.[33] However, the low roughness over an area that is large compared to the particle size indicates that the film topography is generally uniform, with no substantial relief or variance in thickness. The roughness that is observed is due to the curved topography of the particles themselves. This shape effect may be compared with ångström-scale roughness and atomic corrugation in conventional materials.[34]

Mechanical properties were determined quantitatively from the force−displacement curves using custom algorithms written in MATLAB (MathWorks, Natick, MA). The reduced modulus (of the probe and sample) was determined as

$$E_r = \frac{S\sqrt{\pi}}{2\beta\sqrt{A}} \tag{1}$$

where S is the slope of the retract curve as the unloading process begins, depicted in Figure 2a, β is a fitting constant, which is taken to be unity following the procedure in ref 32, and A is the contact area, evaluated using a spherical area function for a probe of known radius R.

Transmission electron microscopy (TEM) was used to characterize the area function of the AFM probe.[35] The radius was determined by fitting a circle to manually selected points at the apex of the probe (Figure 2b). This radius was used to compute the spherical area function used in the measurement of hardness and elastic modulus. The probe was also imaged after scanning, verifying that it was not damaged. The area function was evaluated at a depth $h_{max} - \epsilon P_{max}/S$, where ϵ = 0.75 following the procedure in refs 32 and 36 and P_{max}, S, and h_{max} are defined as shown in Figure 2a.

The plane−strain modulus of the system as defined in eq 1 is a reduced modulus which is a function of the moduli of the materials in contact:

$$\frac{1}{E_r} = \frac{1-\nu_s^2}{E_s} + \frac{1-\nu_p^2}{E_p} \tag{2}$$

where E_s, ν_s, E_p, and ν_p are the Young's modulus and Poisson's ratio of the sample and probe, respectively.[32,36] Because the Poisson's ratio is not known for the present disordered nanoparticle packings, the effective modulus of the sample $E_{eff} = E_s/(1-\nu_s^2)$ will be reported here.

The hardness of the sample was evaluated using the equation

$$H = \frac{P_{max}}{A} \tag{3}$$

where P_{max} is the maximum load encountered during the indent.[32,36]

The loads used in this study are no higher than 800 nN. The authors of refs 32 and 36 intended that both the loads and the depth of indentation are far greater than those used in this study. They consider loads as high as 10 mN to be "very low" for nanoindentation;[37] however, the method has been applied with loads of 100 μN and indentation depths as low as 100 nm on nanoparticle superlattices.[38] Moreover, the valid range of indentation loads and depths are dependent on the indenter size, which here is far smaller than those used in other studies. Similar low-load AFM nanoindentation techniques for uniform surfaces are already in use, for example, PeakForce Tapping,[39] which relies on comparable assumptions but makes use of the Derjaguin−Muller−Toporov (DMT) contact model to evaluate the elastic modulus.[40] PeakForce mode evaluates hardness in a similar fashion to eq 3.

The interpretation of the area function and area of contact has some ambiguity in the present work, because the corrugation resulting from the radii of the nanoparticles (10 nm) is of comparable size to the indentation depth and radius of contact (typically 2−15 nm and 6−18 nm, respectively). The true contact area of an indenter with a homogeneous sample could be interpreted as the area in which, at each point, the normal motion of the surface of the material is exactly equal to that of the indenter tip in contact with that point. By this understanding, it is reasonable to consider the voids between nanoparticles to be part of the contact area as well, which is consistent with the area function as defined here. The methods of Oliver and Pharr were developed for homogeneous, flat samples. Although these packings are flat as compared with the nanoparticle size, they are not homogeneous. For this reason, the reported modulus should be considered an "effective" modulus not only because it is the plane−strain modulus (eq 2), but also because it represents the elastic response of a porous, granular material.

DOI: 10.1021/acs.nanolett.5b05319
Nano Lett. 2016, 16, 2455−2462

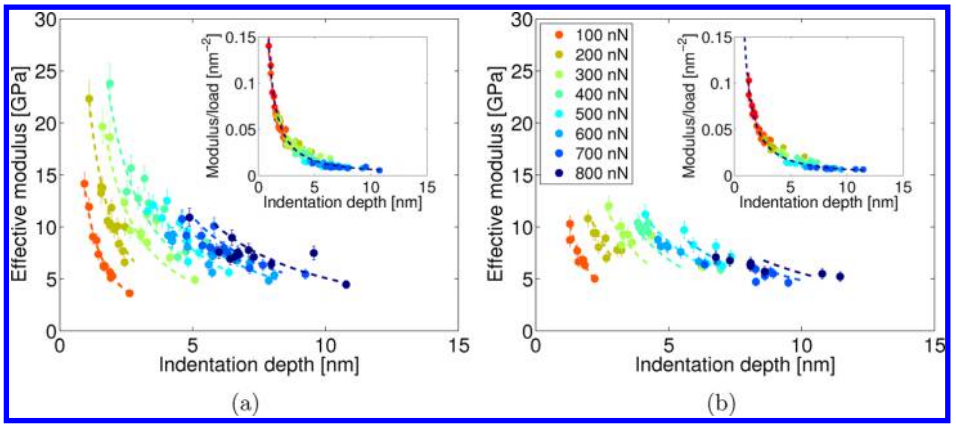

Figure 3. Effective modulus as a function of depth for silica nanoparticle films with thicknesses of 105 nm (a) and 431 nm (b), determined using AFM nanoindentation with various maximum loads P_{max} as shown in the legend. The fits are best fits to $E_{eff} = K_E P_{max}/h_{max}^m$, where K_E and m are fitting parameters. The values of these parameters are presented in Table 1. The insets depict the modulus values normalized by P_{max}, demonstrating how all data points collapse onto a single curve.

Energy dissipation, the unrecovered work done in indenting the material, is evaluated as the cyclic integral of the force curve $\oint P\, dh$.

Topography scans obtained using tapping mode AFM before and after performing indents are used to estimate the affected volume of a single indentation. Figure 1a shows a topography scan taken before a series of indents. Figure 1b shows the result of subtracting the preindent topography scan from the postindent topography scan. The postindent topography scan is visually indistinguishable from the preindent scan, and is provided in Figure S1b for comparison. However, there is a measurable postindent (plastic) displacement. To facilitate the subtraction of pre- and postindent scans to determine this displacement, the pre- and postindent scans are correlated together using a custom image-correlating drift-correction routine. In Figure 1b, the affected region is clearly evident and localized to a single particle. This demonstrates the high spatial resolution of this technique. The slight shading of the surrounding particles indicates a small mismatch in the correlation of the scans, which nonetheless is usually less than 1 nm. Moreover, it shows that the plastic deformation at the surface is confined to the extreme limit of a single particle. Across hundreds of indent sites, the affected region is typically only 1−3 particles.

The effective elastic moduli of the films, as measured using AFM nanoindentation, are plotted against total indentation depth in Figure 3. Each data point is calculated from a single unique indentation at a unique location. The considerable spread in the measured values of modulus and hardness indicates local variations in the film structure (the root-mean-square of the modulus values can be up to 40% of the mean value across a given sample). When a similar investigation was performed on homogeneous poly(methyl methacrylate), no such variation was observed. The accessible range of depths using AFM nanoindentation is from 0 to 20 nm. The insets for each plot show the effective modulus values normalized by the load P_{max}, which collapses the power law fit to a single curve. The uniformity of the data is readily apparent, demonstrating that all of the scatter can be attributed to a single structural degree of freedom in addition to the preselected applied load. We believe this degree of freedom corresponds to the softness or stiffness of the measured region. In addition, the fact that the form of the curve is uniform suggests that the mechanism of yielding is the same regardless of the applied load or stress.

The size of the error bars is determined from uncertainty in the determination of tip radius, which becomes slightly blunted in the course of indentations. The limits of the error bars represent the modulus as evaluated using the tip radius from TEM images before versus after the indentation session. For example, the tip shown in Figure 2b had a radius of 20.6 nm and was measured to be 21.4 nm after a series of 128 indentations. All of the probes used in this study had radii between 16 and 39 nm, and any progressive change in their shapes was recorded. This is believed to be the greatest source of uncertainty in the study, and its effect is always less than 8% for modulus and 16% for hardness. This experimental uncertainty is distinct from the spread in the data, with the latter being a real characteristic of the mechanical properties of the film. The combined effects of both the uncertainty and spread in the data are indicated in the range of moduli given in Table 1.

Table 1. Experimentally-Determined Values of Effective Modulus and the Best-Fit Power Laws Depicted in Figure 3[a]

film thickness	E_{eff} (GPa)	power-law fit	H (GPa)
105 nm	9.3 ± 3.6	$E_{eff} = 0.127 P_{max}/(h_{max})^{1.301}$	1.03 ± 0.51
431 nm	7.8 ± 1.9	$E_{eff} = 0.141 P_{max}/(h_{max})^{1.307}$	0.71 ± 0.24

[a]Displacement for the power law fit is assumed to be nanometers.

Films were studied at ages between 4 days and 6 months from synthesis. The effect of age on mechanical properties will be discussed later, but for consistency all data shown in Figure 3 and Table 1 were collected 4 days after synthesis with the same AFM probe.

The variation in the values of effective modulus is much greater for a thin film of 105 nm (Figure 3a) than for a film with 431 nm thickness (Figure 3b). The effect of film depth on the variance of the effective modulus (shown in Table 1) indicates that the effective modulus is related to film depth—meaning that, in the thinner film, "strong" and "weak" spots exist. We hypothesize that these are related in part to how well particles at the surface can communicate mechanically with the rigid substrate. It is worth emphasizing that each indent is performed to a fixed maximum load, so the range of moduli and

DOI: 10.1021/acs.nanolett.5b05319
Nano Lett. 2016, 16, 2455−2462

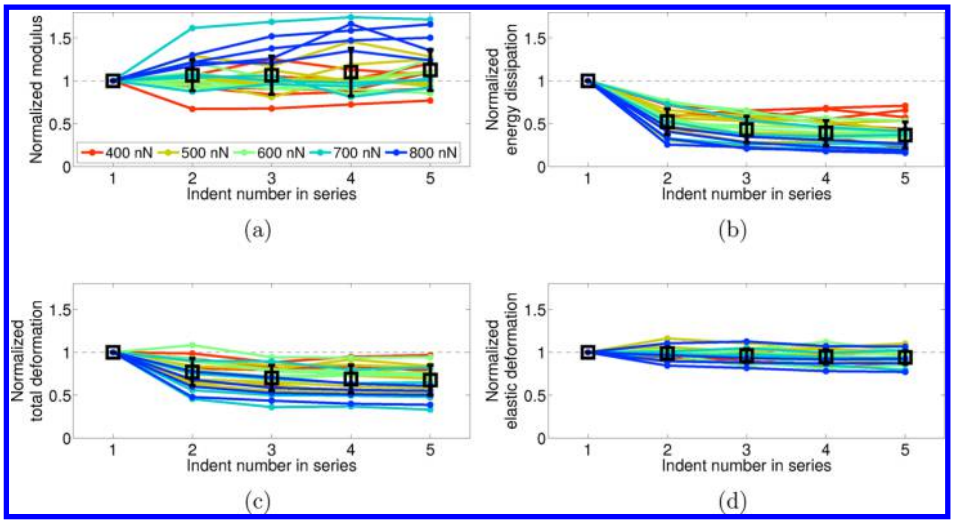

Figure 4. (a) Modulus, (b) energy dissipation, (c) total deformation, and (d) recovered (elastic) deformation for consecutive indents on the same location, normalized to the value for the initial indent. Lines connect data points corresponding to the same location and set of indents. The stiffness increases slightly with compaction, while the energy dissipation and deformation—all measures of plasticity—decrease.

indentation depths indicate the degree to which the film is locally strong or weak. Despite the substantial variance, the data for each film thickness can nevertheless be fit to a single power law of the form $E_{eff} = K_E P_{max}/h_{max}^m$ (Figure 3). In other words, a single pair of values for K_E and m fit all of the data for each film thickness (Table 1). This relationship was chosen based on dimensional analysis: E_{eff} and P_{max}, the only quantities with force dependence, must be linearly related, while the relationship between modulus and indentation depth may vary due the presence of other length scales contributing to the relationship (particle radius, probe radius, and film thickness, although the latter is seen to have no effect on the power law as seen in Table 1).[41]

The effective modulus data fits a power law with $m \approx 1.3$, regardless of the film depth, suggesting that the mechanisms of elastic deformation remain consistent regardless of film thickness. Among various data sets taken on multiple films with multiple probes, the value of m varied in the range $0.9 \leq m \leq 1.35$. However, the power law consistently fits the data set with high accuracy. For example, in the experiments shown here, the 95% confidence intervals are 1.301 ± 0.062 for the 105 nm film and 1.307 ± 0.083 for the 431 nm film. The exponent may vary as a result of varying experimental parameters such as the probe size and shape. However, within a single experiment, the value of m remains remarkably consistent, and all data shown in Figure 3 were collected with the same probe. For the thinner 105 nm film, several outliers with high modulus—still fitting the power law—are visible (Figure 3a) which are not present in the 431 nm film. These stiffer sites only occur for values of P_{max} near the middle of the range investigated. Furthermore, the hardness is closely correlated with the modulus at each site. Typical values of $H/E_{eff} = 0.10 \pm 0.02$, which are comparable to existing data for the yield strain of a range of disordered packings (including colloidal assemblies and metallic glasses)[13] using reasonable estimates for yield stress from hardness.[42] This suggests that these nanoparticle packings also exhibit what has been proposed as a universal mode of cooperative plastic deformation in glassy systems that have the capability for finite plastic flow.[13]

We analyzed the distribution of the effective moduli for 11 experiments, each of which consisted of loads between 100 and 800 nN on 105 nm thick films, performed between 4 and 180 days after synthesis. Error bars indicate the standard deviation of values for a given load and age, with mean values shown by the surface. The best-fit polynomial surface in load/logarithmic time follows the relation (see Figure S3a in the Supporting Information):

$$E_{eff} = 5.22 + 0.0209P_{max} - 2.25 \times 10^{-5}P_{max}^2 + 1.07 \ln(\text{age}) \quad (4)$$

with E_{eff} in GPa, P_{max} in nN, and age in days. This surface is concave down over the range of loads analyzed with confidence $p < 0.05$, further demonstrating that the highest moduli appear for loads in the middle of the range. In addition, the positive coefficient of the ln(age) term shows that the films exhibit slight stiffening with age. The sign of each term in eq 4 is confirmed with confidence $p < 0.05$.

Performing repeated indentations at the same location allows us to separate the effects of elastic and plastic deformation. Representative samples of a series of five indents per site between 400 nN and 800 nN are shown in Figure 4. The measured elastic modulus, dissipated energy, total deformation, and recovered elastic deformation ($h_{max}-h_f$) are plotted in order for each set of five consecutive indents. Each is normalized by the value of the respective parameter on the first indent. (The contact area for all indents was assumed to be equal to that of the first indent. This assumption is necessary because the sample deforms plastically to match the shape of the indenter during the unloading of the first indent, preventing a reasonable evaluation for successive indents. Note that with this assumption, and with load fixed, the hardness $H = P_{max}/A$ remains constant by definition.)

Figure 4 reveals that the dissipated energy is generally highest on the first indent and reduces significantly with successive indents. This energy is proposed to be dissipated through friction between moving particles, indicating that the film rearranges to a more stable configuration under the applied force and retains that position after reloading. The total deformation is seen to decrease almost monotonically for all

DOI: 10.1021/acs.nanolett.5b05319
Nano Lett. 2016, 16, 2455−2462

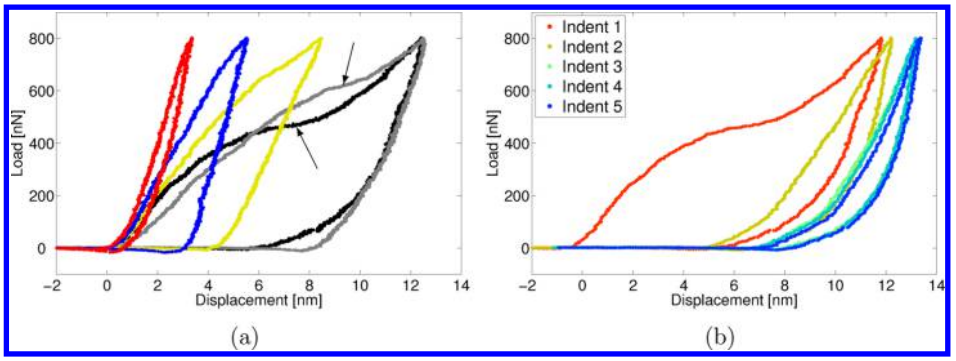

Figure 5. (a) Several force curves to a fixed load of 800 nN representing AFM nanoindentations on various locations on a nanoparticle film, showing the significant variability in curve shape and indent depth. Inflection points characteristic of rearrangements are indicated with arrows in the deepest indents. (b) Several force curves from a repeated indentation on the same site, showing that the retract curves and subsequent approach curves do not overlap.

indents, while the recovered deformation varies nearly randomly. The total deformation is affected by plasticity, and thus is greatest on the first indent, while the recovered deformation reflects only the elastic response from the unload and is relatively unaffected by reloading. This demonstrates that the mechanisms at play are related to particle motion rather than other effects, such as plastic deformation of the tip or particle. The measured elastic modulus (Figure 4a) increases somewhat with reloading (but with significant scatter). This stiffening may be related to compaction of the film. However, because the elastic indentation depth remains relatively constant after the first indent (Figure 4d), it is not expected that the modulus should change significantly.

This study provides unprecedented measurement of the mechanical properties of a disordered nanoparticle packing resolved at the level of the single constituent particles. This permits us to apply load to individual particles and to observe both their local motions (and those of their neighbors) and their mechanical responses. This has not previously been accomplished in a disordered system at this length scale, where the effects of adhesion between the constituent particles are still relevant.

A consistent trend in the data was the significant spatial variation of local modulus. This effect was not present on homogeneous, monolithic reference samples such as rigid silicon and poly(methyl methacrylate). Conventional nanoindentation with a Berkovich indenter was also performed, and this substantial variance was not observed: in conventional nanoindentation, the sampled region is significantly larger, representing an average of tens or hundreds of particles. We thus propose that these regions with lower modulus correspond to preexisting soft spots found at the free surface. Soft spots have already been witnessed to be enhanced in their population at free surfaces in simulations of harmonic spring-connected spheres.[29] The kinks or inflection points in many of the deepest force curves (Figure 5a) indicate that some yielding event took place, which we attribute to rearrangements of nanoparticles in shear transformation zones. The highest values of moduli appear for values of $200 \leq P_{max} \leq 600$ nN, suggesting that the nanoparticle packing rearranges plastically at higher loads to accommodate the indenter tip. Particle motion is observed in the pre- and postindentation scans, especially for loads above 400 nN, as seen in Figure 1.

The relationship between film thickness and measured modulus does not match the standard predictions for substrate effects resulting from nanoindentation on homogeneous thin films.[43,44] Standard predictions assume that indents that are shallow compared to the film depth will have lower measured moduli but the distribution will be wider than for deeper indents,[43] possibly due to surface roughness or uncertainty in the shape of the indenter's blunted end. Conversely, for these nanoparticle packings, the distribution is wider for thinner films as seen in Table 1. The lower end of the modulus distribution is comparable for both 105 and 431 nm films, indicating that "weak" regions are mechanically disconnected from the substrate and independent of film thickness effects. The thinner film has an exaggerated upper bound of its modulus distribution, indicating that "hard" regions are strongly mechanically connected to the substrate, which further demonstrates the structural inhomogeneity of these films. For example, a column of five colinear particles connecting the substrate to the indenter may be mechanically stiff or hard, whereas a region where the nanoparticles are staggered in a zigzag pattern could be soft.[30,45] Note that these structural features do not necessarily imply that the local packing fraction is greater in the vicinity of a hard region.

The observed relationship between maximum applied load and measured modulus—wherein the loads between 200 nN and 600 nN produced the stiffest material response—was confirmed valid across 11 similar data sets with $p < 0.05$ confidence. This distribution is independent of the observed aging effects. A homogeneous, linear material should exhibit a uniform elastic modulus at every location, regardless of the load. That this material exhibits both an increasing modulus trend with increasing load at low loads, and a decreasing modulus with load at higher loads, indicates that at least two nonlinear deformation mechanisms must be at play. We postulate that the lower-load mechanism is that of jamming, as the system compacts under the load.[12,46] The higher-load mechanism is proposed to be a yielding mechanism which softens the material under adequate stress, as mentioned previously. This deformation takes the form of particle rearrangements and may correspond to the activation of shear transformation zones.[15] Fluid cell ellipsometry was used to measure the porosity of the films, and the packing fraction was determined to be $0.70 \leq \Phi \leq 0.81$.[4] This range of values is significantly greater than the predicted value $\Phi \approx 0.64$ for random jammed packing of monodisperse spheres[46] but is typical of measured values for nanoparticle packings.[47] It is likely that the discrepancy between the measured value and the predicted value is due to the polydispersity of the spheres, thin alumina coating, and random error in the method. Never-

DOI: 10.1021/acs.nanolett.5b05319
Nano Lett. 2016, 16, 2455−2462

theless, the present packings are likely very close to the jamming transition, such that they jam locally when a load of 200−600 nN is applied to a single particle.

Films exhibited a small but measurable stiffening behavior as they aged from 4 to 180 days from synthesis, as shown in eq 4 and Figure S3 in the Supporting Information. This stiffening behavior may be attributed to the formation of either hydrogen bonds or oxide bridges between nanoparticles, as the surfaces of the alumina-coated particles are expected to possess a significant density of −OH groups. Molecular dynamics simulations have previously revealed aging in silanol-terminated silica surfaces, albeit over a shorter time scale.[48] Strengthening behavior (increasing static friction) with time has been observed in friction experiments for time scales of up to days in macroscopic tests,[49] and over shorter time scales (seconds) in nanoscale single asperity contact tests.[50] These nanoparticles are coated with alumina. We hypothesize that Al−O−Al bridges form over time, which makes the particles more strongly bound.

The behavior witnessed in Figure 5b is not expected for an ideal elastoplastic material. For such a material, if the indenter is reloaded, the reloading portion of the force curve for the subsequent indent should exactly match the withdrawal portion of the previous one.[36] Here the curves do not overlap (Figure 5b). This indicates some energy dissipation mechanism which is at play during the retraction and reloading. This is plausibly due to interparticle friction, as has been witnessed previously in nanoindentation on nanoparticle packings.[23] This also explains why the energy dissipation does not drop all the way to zero in Figure 4b, as would otherwise be expected. This type of interparticle friction has been observed in granular packings at larger scales.[30,51] Further study into the nature of adhesion and friction between the nanoparticles is warranted; experiments to further investigate these interactions are under development in our laboratory.

The major difference between "stiff" and "soft" force curves lies in their shapes, as seen in Figure 5a. Regions identified as "stiff" behave in a nearly hard-wall or homogeneous fashion, as shown in the red and blue curves. "Soft" regions exhibit much deeper indents. The gray and black curves both exhibit inflection points at depths of 7−10 nm, which is comparable to the particle radius. This indicates that a local, plastic rearrangement of nanoparticles has taken place, and the rearrangements can sometimes be identified in the topography scans taken before and after indents (Figure 1b).

It is challenging to accurately calculate the density of soft spots in the present material. However, a rough estimate can be made from the size and depth of the indentation sites, and an estimate of the fraction of indentation sites at which rearrangements occur. From the difference topography image in Figure S1c, it can be estimated that rearrangements are 1−3 particles in size on the surface, and from the depth of the force curves in Figure 5a, which is on the order of one particle radius, the depth is approximately two particles. Thus, we estimate that 4−6 particles are involved in a rearrangement in this system. If 10% of the sites are soft—again judging from the difference image and Figure 3—then the soft spot density is approximately one per 40−60 particles. This value falls within the wide range of amorphous material defect densities reported elsewhere.[24,25,29,52] The value we determine may be affected by the properties of the present system, including its packing fraction which is below jamming, the threshold for softness that we used, and the fact that our technique only probes particles within a few diameters of a free surface, where soft spots are known to have an enhanced population.[29]

The mechanical properties of silica nanoparticle packings have been measured using AFM nanoindentation. It has been shown that these films are mechanically inhomogeneous, and the measured effective elastic modulus varies by up to 80% at different locations. However, despite this large spread, the elastic modulus has a clear power-law dependence on maximum load and depth at all locations. The observed displacements at the single particle level combined with the measured force−displacement response supports a picture where plasticity is related to rearrangements of a few particles, in accordance with the stress-driven shear transformation zone theory in amorphous materials. The observed failure strain is consistent with that observed for other disordered packings. This response is markedly distinct from that expected for crystalline arrangements which accommodate flow via dislocation motion. These results are useful in the design of nanoparticle coatings, especially those with a functional mechanical application. They may also assist in the ongoing search for toughening mechanisms of disordered packings. Specifically, because plasticity likely originates at soft spots, it is expected that they contribute to ductility. Therefore, materials designed using processing routes which enhance the sizes or concentrations of soft spots may be less susceptible to fracture.

Atomic force microscopy has also demonstrated mechanical heterogeneity in metallic glasses,[19] lending credence to the idea that nanoparticle films are effective analogs for atomic glasses. This is especially true for those amorphous materials with isotropic bonding configurations, such as metallic glasses, colloidal suspensions, and granular packings, particularly those that are bound by adhesive forces between the particles. The spatial variability of mechanical properties demonstrated here, and their structural dependence, are potentially exhibited in many of these systems as well.

■ ASSOCIATED CONTENT

Supporting Information

The Supporting Information is available free of charge on the ACS Publications website at DOI: 10.1021/acs.nanolett.5b05319.

The pre- and postindent topography images and the complete difference image from Figure 1, electron micrographs of the probe shown in Figure 2b after performing indentations, a summary of the settings and parameters used in topography mode scanning, a figure depicting the distribution of data described by eq 4, sample force−displacement curves performed on a homogeneous polymer, and a plot of modulus vs depth including several data points on thinner films not mentioned in the present paper (PDF)

■ AUTHOR INFORMATION

Corresponding Author

*E-mail: carpick@seas.upenn.edu. Phone: +1 (215) 898-4608. Fax: +1 (215) 573-6334.

Present Addresses

T.D.B.J.: Department of Mechanical Engineering & Materials Science, University of Pittsburgh, Pittsburgh, PA 15261.

Y.-R.H.: Department of Chemical Engineering, Carnegie Mellon University, Pittsburgh, PA 15213.

DOI: 10.1021/acs.nanolett.5b05319
Nano Lett. 2016, 16, 2455−2462

Notes

The authors declare no competing financial interest.

■ ACKNOWLEDGMENTS

The authors thank Profs. Dan Gianola, Andrea Liu, Don Stone, and Gang Feng for helpful discussions. Use of the facilities of Nano/Bio Interface Center and the Nanoscale Characterization Facility at the University of Pennsylvania are acknowledged. We acknowledge support by the UPENN MRSEC, NSF Grant No. DMR-1120901, and funding from the Ashton Foundation (J.L.).

■ REFERENCES

(1) Sharma, P.; Kaushik, N.; Kimura, H.; Saotome, Y.; Inoue, A. *Nanotechnology* **2007**, *18*, 035302.
(2) Schroers, J.; Nguyen, T.; O'Keeffe, S.; Desai, A. *Mater. Sci. Eng., A* **2007**, *449*−*451*, 898−902.
(3) Lettington, A. H. *Carbon* **1998**, *36*, 555−560.
(4) Lee, D.; Rubner, M. F.; Cohen, R. E. *Nano Lett.* **2006**, *6*, 2305−12.
(5) Park, J. T.; Kim, J. H.; Lee, D. *Nanoscale* **2014**, *6*, 7362−68.
(6) Löffler, J. F. *Intermetallics* **2003**, *11*, 529−540.
(7) Liu, L.; Qiu, C. L.; Huang, C. Y.; Yu, Y.; Huang, H.; Zhang, S. M. *Intermetallics* **2009**, *17*, 235−240.
(8) Ma, M. Z.; Liu, R. P.; Xiao, Y.; Lou, D. C.; Liu, L.; Wang, Q.; Wang, W. K. *Mater. Sci. Eng., A* **2004**, *386*, 326−330.
(9) Ishida, M.; Takeda, H.; Nishiyama, N.; Kita, K.; Shimizu, Y.; Saotome, Y.; Inoue, A. *Mater. Sci. Eng., A* **2007**, *449*−*451*, 149−154.
(10) Shipway, A. N.; Willner, I. *Chem. Commun.* **2001**, *20*, 2035−2045.
(11) Silbert, L. E.; Liu, A. J.; Nagel, S. R. *Phys. Rev. Lett.* **2005**, *95*, 098301.
(12) Liu, A. J.; Nagel, S. R. *Annu. Rev. Condens. Matter Phys.* **2010**, *1*, 347−369.
(13) Strickland, D. J.; Huang, Y.-R.; Lee, D.; Gianola, D. S. *Proc. Natl. Acad. Sci. U. S. A.* **2014**, *111*, 18167−72.
(14) Manning, M. L.; Liu, A. J. *Phys. Rev. Lett.* **2011**, *107*, 108302.
(15) Argon, A. S. *Acta Metall.* **1979**, *27*, 47−58.
(16) Cao, P.; Lin, X.; Park, H. S. *Phys. Rev. E* **2014**, *90*, 012311.
(17) Argon, A. S.; Shi, L. T. *Philos. Mag. A* **1982**, *46*, 275−294.
(18) Schall, P.; Weitz, D. A.; Spaepen, F. *Science* **2007**, *318*, 1895−1899.
(19) Liu, Y. H.; Wang, D.; Nakajima, K.; Zhang, W.; Hirata, A.; Nishi, T.; Inoue, A.; Chen, M. W. *Phys. Rev. Lett.* **2011**, *106*, 125504.
(20) Zeng, J. F.; Chu, J. P.; Chen, Y. C.; Volland, A.; Blandin, J. J.; Gravier, S.; Yang, Y. *Intermetallics* **2014**, *44*, 121−127.
(21) Cao, A. J.; Cheng, Y. Q.; Ma, E. *Acta Mater.* **2009**, *57*, 5146−5155.
(22) Greer, A. L.; Cheng, Y. Q.; Ma, E. *Mater. Sci. Eng., R* **2013**, *74*, 71−132.
(23) Zhang, L.; Feng, G.; Zeravcic, Z.; Brugarolas, T.; Liu, A. J.; Lee, D. *ACS Nano* **2013**, *7*, 8043−8050.
(24) Li, W.; Bei, H.; Tong, Y.; Dmowski, W.; Gao, Y. F. *Appl. Phys. Lett.* **2013**, *103*, 171910.
(25) Li, W.; Gao, Y.; Bei, H. *Sci. Rep.* **2015**, *5*, 14786.
(26) Lee, D.; Jia, S.; Banerjee, S.; Bevk, J.; Herman, I. P.; Kysar, J. W. *Phys. Rev. Lett.* **2007**, *98*, 026103.
(27) Dafinone, M. I.; Feng, G.; Brugarolas, T.; Tettey, K. E.; Lee, D. *ACS Nano* **2011**, *5*, 5078−87.
(28) Zhang, L.; Prosser, J. H.; Feng, G.; Lee, D. *Nanoscale* **2012**, *4*, 6543−52.
(29) Sussman, D. M.; Goodrich, C. P.; Liu, A. J.; Nagel, S. R. *Soft Matter* **2015**, *11*, 2745−2751.
(30) Bassett, D. S.; Owens, E. T.; Porter, M. A.; Manning, M. L.; Daniels, K. E. *Soft Matter* **2015**, *11*, 2731−2744.
(31) Prosser, J. H.; Brugarolas, T.; Lee, S.; Nolte, A. J.; Lee, D. *Nano Lett.* **2012**, *12*, 5287−91.
(32) Oliver, W. C.; Pharr, G. M. *J. Mater. Res.* **2004**, *19*, 3−20.
(33) Chen, Y.; Huang, W. *Meas. Sci. Technol.* **2004**, *15*, 2005−2010.
(34) Mate, C. M. *Tribology on the Small Scale*; Oxford University Press: Oxford, 2008.
(35) Jacobs, T. D. B.; Wabiszewski, G. E.; Goodman, A. J.; Carpick, R. W. *Rev. Sci. Instrum.* **2016**, *87*, 013703.
(36) Oliver, W. C.; Pharr, G. M. *J. Mater. Res.* **1992**, *7*, 1564−1583.
(37) Page, T. F.; Oliver, W. C.; McHargue, C. J. *J. Mater. Res.* **1992**, *7*, 450−473.
(38) Tam, E.; Podsiadlo, P.; Shevchenko, E.; Ogletree, D. F.; Delplancke-Ogletree, M.-P.; Ashby, P. D. *Nano Lett.* **2010**, *10*, 2363−67.
(39) Pittenger, B.; Erina, N.; Su, C. Quantitative Mechanical Property Mapping at the Nanoscale with PeakForce QNM.
(40) Derjaguin, B. V.; Muller, V. M.; Toporov, Y. P. *J. Colloid Interface Sci.* **1975**, *53*, 314−326.
(41) Cheng, Y. T.; Cheng, C. M. *Mater. Sci. Eng., R* **2004**, *44*, 91−149.
(42) Marsh, D. M. *Proc. R. Soc. London, Ser. A* **1964**, *279*, 420−435.
(43) Tsui, T. Y.; Pharr, G. M. *J. Mater. Res.* **1999**, *14*, 292−301.
(44) Clifford, C. A.; Seah, M. P. *Nanotechnology* **2006**, *17*, 5283−5292.
(45) Majmudar, T. S.; Behringer, R. P. *Nature* **2005**, *435*, 1079−1082.
(46) O'Hern, C. S.; Silbert, L. E.; Liu, A. J.; Nagel, S. R. *Phys. Rev. E: Stat. Phys., Plasmas, Fluids, Relat. Interdiscip. Top.* **2003**, *68*, 011306.
(47) Cook, K. T.; Tettey, K. E.; Bunch, R. M.; Lee, D.; Nolte, A. J. *ACS Appl. Mater. Interfaces* **2012**, *4*, 6426−6431.
(48) Liu, Y.; Szlufarska, I. *Phys. Rev. Lett.* **2012**, *109*, 186102.
(49) Ruina, A. *J. Geophys. Res.* **1983**, *88*, 10359−10370.
(50) Li, Q.; Tullis, T. E.; Goldsby, D.; Carpick, R. W. *Nature* **2011**, *480*, 233−236.
(51) Landry, J. W.; Grest, G. S.; Silbert, L. E.; Plimpton, S. J. *Phys. Rev. E: Stat. Phys., Plasmas, Fluids, Relat. Interdiscip. Top.* **2003**, *67*, 041303.
(52) Rottler, J.; Schoenholz, S. S.; Liu, A. J. *Phys. Rev. E* **2014**, *89*, 042304.

DOI: 10.1021/acs.nanolett.5b05319
Nano Lett. 2016, 16, 2455−2462